Aeroacoustics Conferences
26-29 May 2026, Brussels, Belgium
32nd AIAA/CEAS Aeroacoustics Conference (2026)

10.2514/6.2026-3457

Experimental Study on Sound Propagation through a Duct Section with Large Pylons

Maximilian Behn * and Ulf Tapken †
German Aerospace Center (DLR), Institute of Propulsion Technology, Berlin, Germany

Hugo Vincent ‡, Antonio Pereira §, and Marc C. Jacob ¶
Ecole Centrale de Lyon, CNRS, Univ Claude Bernard Lyon 1, INSA Lyon, LMFA, UMR5509, 69130, Ecully, France

The pressure distribution of an acoustic mode emitted into the bypass duct of an aeroengine is significantly altered by the pylons' boundary conditions. The presented experimental study aims to analyze the associated propagation effects in detail. For this purpose, large pylons are installed in an annular duct section and subjected to individual modes of controlled propagation angles. The modes are generated by a spinning mode generator consisting of two loudspeaker rings, which is operated in such a way that all modes of other azimuthal and radial orders are effectively suppressed. The transmitted, scattered and reflected fractions of the incident mode are measured using mode detection microphone arrays in the upstream annular duct and in the pylon section. To account for the impact of the pylons' shape on the mode propagation in the inter-pylon duct the radial mode decomposition technique is extended accordingly. The results demonstrate that the incident mode perceives the propagation conditions of the inter-pylon section in a distinctly different manner depending on the angle of incidence. This leads to diverse transmission behavior and manifests itself in the form of various mode orders being generated in the inter-pylon ducts. At the trailing edge of the pylon section, the resulting sound pressure distribution is dominated either by the order of the incident mode, its inverse order, or by a scattering mode.

I. Introduction

The aft-radiated noise from the bypass duct of aircraft engines is composed of dominant tonal components at the blade passing frequency and its harmonics caused by the interaction of the fan rotor wakes and the stator vanes. The sound generated propagates as spinning modes both upstream and downstream of the fan stage, for which distinct mode orders result according to the Tyler-Sofrin rule [1]. Due to the higher bypass ratio in Ultra-High Bypass Ratio (UHBR) engines, the relative contribution of fan noise (tonal and broadband) to the overall radiated sound is expected to increase in comparison to jet noise [2]. In order to reduce noise immission in the vicinity of airports in compliance with ICAO regulations, the knowledge of directivity and strength of far-field radiated fan noise is important to identify required noise mitigation measures. In the bypass duct, the bifurcation created by the upper and lower pylon (or strut) causes scattering and reflection of the incident modes. As the modes propagate further downstream through the duct between neighboring pylons, they are reflected by the pylons and scattered into several modes in the inter-pylon ducts [3–5]. The scattered modes contribute to the far-field radiation resulting in complex directivity patterns [6, 7]. If the pylons are positioned close to the fan stator or are even integrated into the stator row, the upstream effect of the pylons can influence the flow incidence at the stator vanes causing the excitation of additional modes apart from the azimuthal mode orders according to the Tyler-Sofrin rule [8, 9]. It is of equal significance for the design of acoustic liners in the bypass duct to take mode scattering at the pylons into account [10].

Thus far, very few measurements of the mode propagation through the inter-pylon duct have been reported [11–13]. In each investigation microphone arrays were placed outside of the pylon section. In a recent study, an experimental setup has been equipped with large pylons to investigate mode propagation effects through duct installations [14, 15].

*Research Engineer, Engine Acoustics Department, Bismarckstraße 101, 10625 Berlin, Germany, Member AIAA, maximilian.behn@dlr.de
†Research Scientist, Engine Acoustics Department, Bismarckstraße 101, 10625 Berlin, Germany, ulf.tapken@dlr.de
‡Post-doctoral fellow, Ecole Centrale de Lyon, Laboratoire de Mécanique des Fluides et d'Acoustique, France, hugo.vincent@ec-lyon.fr
§Research Engineer, Ecole Centrale de Lyon, Laboratoire de Mécanique des Fluides et d'Acoustique, France, antonio.pereira@ec-lyon.fr
¶Professor, Ecole Centrale de Lyon, Laboratoire de Mécanique des Fluides et d'Acoustique, France, Member AIAA, marc.jacob@ec-lyon.fr

Two configurations comprising, respectively, two and three symmetrically arranged, large pylons were tested over a broad range of mode orders and excitation frequencies. A loudspeaker array served as spinning mode generator allowing the generation of single, dominant target modes. The incoming, reflected and scattered sound field was measured using a microphone array in the annular duct section between the spinning mode generator and the pylons. Another microphone array was located inside the inter-pylon ducts close to the pylons' trailing edges, which detects the transmitted and scattered modes as well as reflected modes from the pylon trailing edges. The same setup is investigated numerically by Vincent et al. [16] considering the effect of mean flow and analytically by Girier et al. [17] employing a mode-matching procedure. The objective is to determine the sound power transfer between the annular duct modes and the inter-pylon duct modes in relation to the mode propagation angle and the number of pylons. Therefore, radial mode analysis is extended by accounting for mode propagation in ducts with axially varying, circumferential boundaries.

In the following, the experimental setup is introduced. Mode propagation in annular and c-shaped ducts is described with focus on the mode propagation angle. Subsequently, azimuthal mode analysis and radial mode analysis using microphone arrays are presented for annular and c-shaped, hard-walled ducts. These analysis techniques are applied to the measured sound fields and the results are discussed regarding the impact of the pylons on the mode propagation.

II. Experimental setup

For the present study, the SPIN test bench (Spinning mode Propagation through INstallations in flow ducts, previously called MoSy) was equipped with two and three pylons with an overall length of 1.5 duct diameters as shown in Fig. 1. The duct has an outer radius of 0.25 m and a hub radius of 0.165 m. While it is possible to perform measurements with mean background flow being generated by a fan attached to one of the quasi-anechoic terminations, the measurements presented here were conducted without flow. A spinning mode generator consisting of two rings with 16 loudspeakers each was installed. The driving signals are adjusted for each loudspeaker individually in amplitude and phase in order to generate single, dominant modes and suppress all other cut-on modes in the range of azimuthal orders $m_a \in \{-7, \ldots, +7\}$* and radial orders $n \in \{0, 1\}$ [18]. By controlling the modes of the incident sound field, reflection, transmission and scattering at a test object can be measured accurately for each mode order. Pylons with an overall length of $L = 0.75$m and NACA 0015 profile were manufactured in 3D printing. Configurations with two and three symmetrically arranged pylons were tested for frequencies between 400 and 3200 Hz (corresponding to $kL \approx 5.5$ to 44) and various cut-on modes. The dataset comprises 284 measurements for 19 different mode orders, that include 155 test points for the two-pylon configuration and 129 test points for the three-pylon configuration. Two microphone arrays were installed, one in the annular duct between the spinning mode generator and the pylon section and the other in the pylon section close to the trailing edges. The microphone arrays consist each of 98 1/4"' high quality G.R.A.S. condenser microphones, which were arranged in a ring with 33 uniformly spaced sensor positions and 5 sparse ring arrays with 13 irregularly spaced microphones that was optimized for Compressed Sensing based Azimuthal Mode Analysis [14].

The microphone positions in the inter-pylon ducts are shown in Fig. 2 for both configurations. The axial sensor positions are given relative to the pylon leading edges. Because of the uneven number of microphones in the ring array, the ring arrays in both inter-pylon ducts in Fig. 2a are not symmetric with respect to the pylon walls. Also the positions of one of the axial line arrays are covered by a pylon, resulting in one microphone line array in each inter-pylon duct. For the case of three pylons, Fig. 2b shows that sensors of the microphone ring are installed directly at the walls of each pylon. Additionally, one inter-pylon duct is equipped with symmetrically arranged microphone line arrays, which enable the measured sound field to be decomposed into radial modes. The location of this microphone array in the inter-pylon duct represents a particularity of the experimental setup, because radial mode decomposition is performed in the inter-pylon ducts with axially varying cross-section. The apex angle ϕ_a between neighboring pylons is shown in Fig. 3 over the pylon chord length for the three pylon configuration. The apex angle varies by about 26 degrees from its largest extent at the leading and trailing edge to the point of maximum thickness located at 30% of the chord length. At the microphone array the apex angle increases almost linearly by approximately 1.65 degrees from one microphone position to the next one. For the two pylon configuration, the apex angle increases by 60 degrees in comparison to Fig. 3.

*The azimuthal mode order is typically denoted by m. Here, m_a is used to distinguish the mode order in the annular duct from the mode order m_c in the inter-pylon ducts.

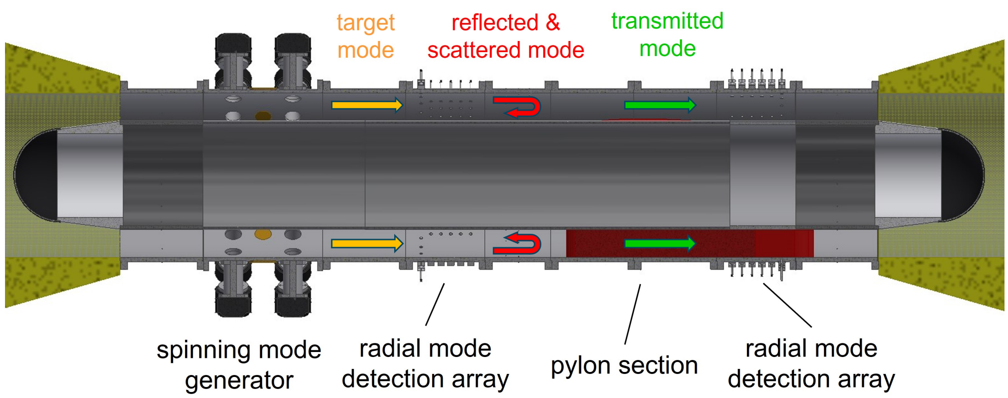

Fig. 1 Experimental setup of the SPIN test bench for investigating mode propagation through pylon sections for single, dominant modes that are generated by a loudspeaker array (spinning mode generator). The resulting sound field is measured with radial mode detection arrays.

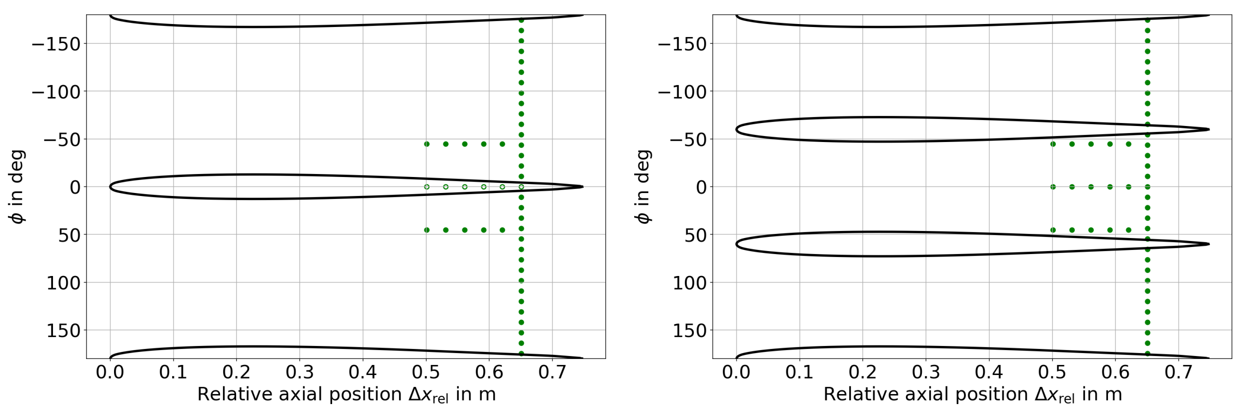

(a) Two pylon configuration (b) Three pylon configuration

Fig. 2 Microphone positions relative to the pylon leading edge indicated by green dots for both configurations.

III. Mode propagation in the inter-pylon duct

Sound propagation inside a hard-walled duct, which is filled with a quiescent medium, is governed by the Helmholtz equation in cylindrical coordinates [19]. The solution of this equation is obtained by application of a separation approach of the form $X(x)R(r)\Phi(\phi)$ and yields:

$$p(x,r,\phi,t) = \sum_{m=-\infty}^{+\infty} \sum_{n=0}^{+\infty} \left(A_{mn}^{+} X_{mn}^{+}(x) + A_{mn}^{-} X_{mn}^{-}(x) \right) R_{mn}(r) \Phi_m(\phi) e^{-i\omega t}. \tag{1}$$

The individual terms of the double sum in Eq. (1) are denoted as modes with mode amplitudes $A_{mn}^{\pm}$ propagating in positive (+) and negative (−) axial direction. The modes are characterised by the azimuthal mode order m and radial mode order n. Next, the respective mode shape functions $X_{mn}^{\pm}$, R_{mn} and Φ_m are derived for annular and c-shaped ducts.

A. Mode propagation in annular ducts

The boundaries in an annular duct apply to the radial mode shape function $R_{m_a n}$ such that the radial pressure derivative $\partial p/\partial r = \mathrm{d}R_{m_a n}/\mathrm{d}r$ vanishes at the inner and outer duct wall as a result of zero radial velocity. The radial mode shape function then yields

$$R_{m_a n}(r) = \frac{1}{\sqrt{F_{a,m_a n}}} \left(J_{m_a}(\sigma_{m_a n} r/R_o) + Q_{m_a n} Y_{m_a}(\sigma_{m_a n} r/R_o) \right) =: f_{m_a n}(r), \tag{2}$$

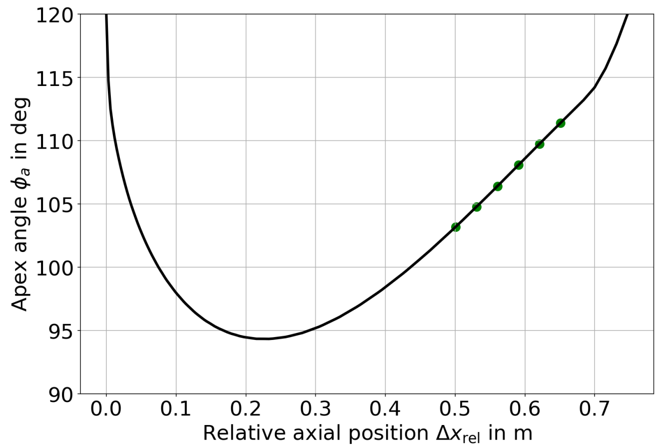

Fig. 3 Axial variation of the apex angle of the inter-pylon ducts along the pylon chord length for three pylons. The apex angle is evaluated at the outer duct wall. The axial microphone positions are indicated by green dots.

which is a linear combination of Bessel functions of first and second kind of order m_a. The eigenvalues $\sigma_{m_a n}/R_o$ and $Q_{m_a n}$ are obtained by solving the resulting equations at the duct boundaries. The normalisation factor $F_{a,m_a n}$ for the annular duct ensures that mode amplitudes are comparable between differing radial orders [18]. The azimuthal mode shape function is governed by the differential equation

$$\frac{\mathrm{d}^2\Phi_{m_a}}{\mathrm{d}\phi^2} + m_a^2\Phi_{m_a} = 0, \tag{3}$$

which is solved by

$$\Phi_{a;m_a}(\phi) = e^{im_a\phi}. \tag{4}$$

Finally, the axial mode propagation is described by

$$X^{\pm}_{m_a n}(x) = e^{ik^{\pm}_{m_a n}x} \tag{5}$$

with the axial wavenumber

$$k^{\pm}_{m_a n} = \pm\alpha_{m_a n}k. \tag{6}$$

The mode propagation factor $\alpha_{m_a n} = \sqrt{1 - \sigma^2_{m_a n}/(kR_o)^2}$ depends on the mode order and free-field wavenumber $k = \omega/c$. It is zero at the mode cut-on frequency and increases asymptotically to the value 1 with increasing frequency. The mode propagation angle with respect to the duct axis (x-axis) is directly linked to the mode propagation factor:

$$\zeta^{\pm}_{\mathrm{x};m_a n} = \arccos\left(\pm\alpha_{m_a n}\right). \tag{7}$$

The acoustic modes are mutually orthogonal facilitating the determination of mode sound power given as:

$$P^{\pm}_{m_a n} = \alpha_{m_a n}\frac{\pi R_o^2}{\rho c}|A^{\pm}_{m_a n}|^2. \tag{8}$$

B. Integration of hardwall boundaries in azimuthal direction

The duct between two neighboring pylons can be approximated by a so-called c-shaped duct assuming duct boundaries are placed at constant azimuthal positions ϕ_+ and ϕ_-. The apex angle of a c-shaped duct is $\phi_a = \phi_+ - \phi_-$. In case of bifurcated ducts, this simplification is feasible for sufficiently large hub-to-tip ratios, where the maximum deviation between the boundaries of the assumed c-shaped duct and the actual inter-pylon duct is small, see Fig. 4. Imposing hardwall boundaries to the differential equation for the azimuthal mode shape function in Eq. (3) yields

$$\Phi_{c;m_c}(\phi) = \cos\left(m_c \cdot \frac{\pi}{\phi_a}\phi\right), \tag{9}$$

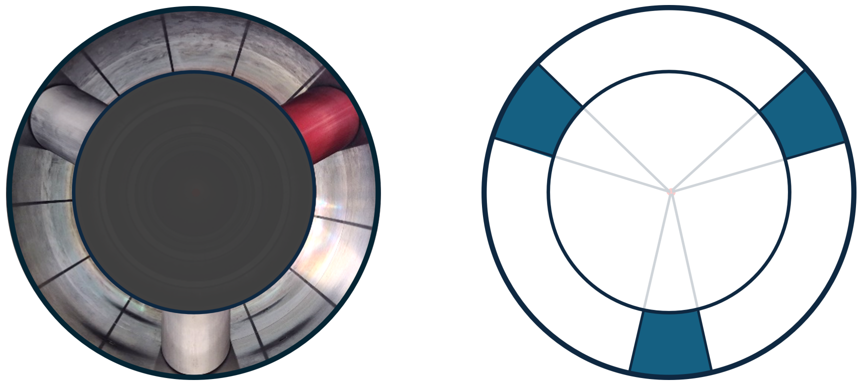

(a) Inter-pylon duct (b) C-shaped duct

Fig. 4 Simplification of the inter-pylon ducts formed by neighboring pylons with radially constant thickness (a) to c-shaped ducts (b).

where the coordinate ϕ applies to a local coordinate system with boundaries at $\phi_+ = \phi_a$ and $\phi_- = 0$. The azimuthal mode shape describes a standing wave pattern with $m_c \geq 0$. The change in the azimuthal mode order from m_a to $m_c \cdot \frac{\pi}{\phi_a}$ also affects the radial mode shape function through a change in the order of the Bessel functions and hence, of the eigenvalues. As a result, the axial wavenumber changes according to Eq. (6). Despite $m_c \cdot \frac{\pi}{\phi_a}$ being the effective azimuthal mode order, it is practical to use the azimuthal mode order m_c for the subscripts of all related variables like mode amplitude and mode sound power.

Due to the additional duct boundaries, the normalization factor $F_{c,m_c n}$ for c-shaped ducts is adapted accordingly:

$$F_{c,m_c n} = \begin{cases} F_{a,m_c n} & \text{if } m_c = 0 \\ \sqrt{2} F_{a,m_c n} & \text{if } m_c \geq 1 \end{cases} \tag{10}$$

The resulting mode sound power propagated inside a c-shaped duct is computed similarly to the annular duct case as

$$P^{\pm}_{m_c n} = \alpha_{m_c n} \frac{\phi_a R_o^2}{2\rho c} |A^{\pm}_{m_c n}|^2. \tag{11}$$

When a mode in the annular duct section impinges onto the pylon section, it scatters partly into inter-pylon duct modes. The amplitude distribution of the scattered modes can be estimated by projecting the azimuthal mode shapes in the annular duct $\Phi_{a;m_a}(\phi)$ (see Eq. (4)) onto the azimuthal mode shapes in the inter-pylon duct $\Phi_{c;m_c}(\phi)$ (see Eq. (9)), where m_a indicates the azimuthal mode order in the annular duct and m_c in the c-shaped duct:

$$F_{m_a \to m_c} = \left| \frac{1}{\phi_a} \int_0^{\phi_a} \Phi_{a;m_a}(\phi) \cdot \Phi_{c;m_c}(\phi) \mathrm{d}\phi \right| \tag{12}$$

$$= \left| \frac{1}{\phi_a} \int_0^{\phi_a} e^{i m_o \phi} \cdot \cos\left(m_c \frac{\pi}{\phi_a} \phi \right) \mathrm{d}\phi \right|. \tag{13}$$

The scattering distribution according Eq. (13) is evaluated for the two pylon ($N_{\text{pylon}} = 2$) and three pylon ($N_{\text{pylon}} = 3$) configuration applying the maximum apex angle $\max(\phi_a) = \frac{2\pi}{N_{\text{pylon}}}$, which is valid at the pylon leading and trailing edge. The results in Fig. 5 show that except for $m_a = 0$ each annular duct scatters into several inter-pylon duct modes, with two distinct azimuthal mode orders m_c being dominant for each azimuthal mode orders m_a. This simplified analysis of the scattering patterns should be compared with the experimental results in Section V.C, which were measured after propagation through the inter-pylon duct at the downstream array.

The range of cut-on modes depends on the apex angle ϕ_a. Due to the pylons' varying thickness a mode can have two transition points in the inter-pylon ducts as illustrated in Fig. 6. A downstream propagating mode first turns cut-off at the left transition point, where it decays exponentially as it approaches the narrow section of the inter-pylon duct.

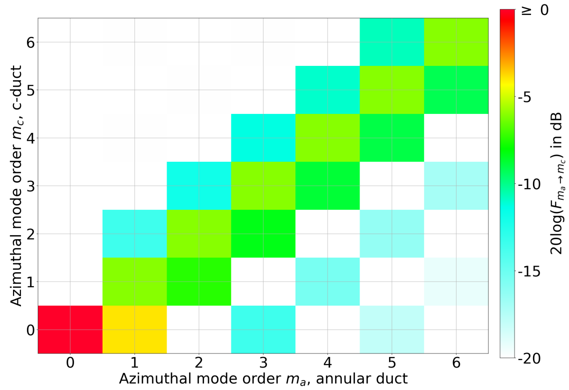

(a) Two pylon configuration, max(ϕ_a) = 180 deg

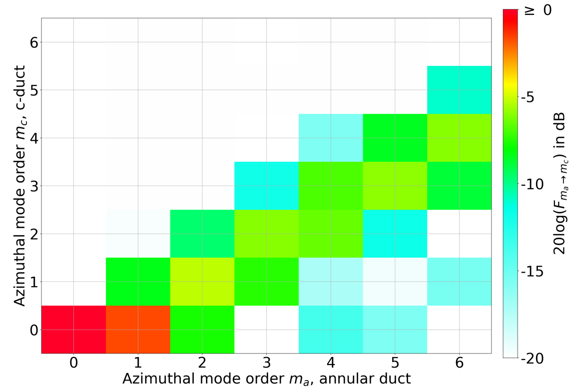

(b) Three pylon configuration, max(ϕ_a) = 120 deg

Fig. 5 Projection of the azimuthal mode shapes of annular duct modes onto the azimuthal mode shapes of c-shaped duct modes according to Eq. (13)**.**

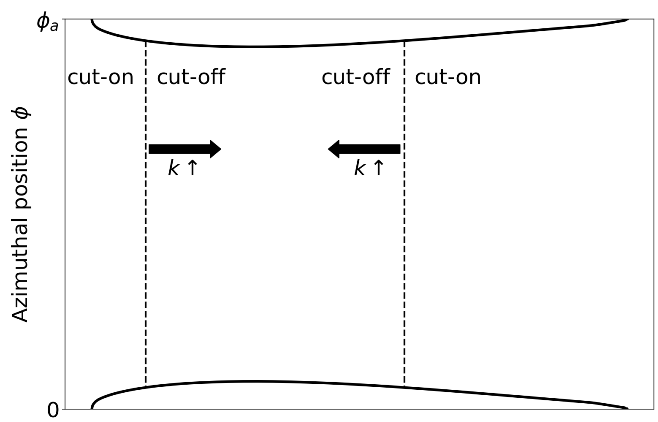

Fig. 6 Double transition points located at positions of equal apex angle that converge with increasing frequency.

Downstream of the point of maximum thickness, i.e. 30% relative chord length for NACA 0015 profile, a second transition point from cut-off to cut-on exists at the position, where the local apex angle is equal to the apex angle at the first transition point. With increasing frequency the transition points shift to positions with smaller local apex angle. When both transition points merge, the mode is cut-on in the entire inter-pylon duct. The interested reader is advised to read the article by Girier et al. [17] for further details on mode propagation in the inter-pylon duct.

C. Slowly-varying duct with azimuthal boundaries

The azimuthal width of the inter-pylon ducts varies in axial direction due to the pylons' shape. If the rate of change is assumed to be small in comparison to the mode wavelength, a slowly-varying duct approach can be sought based on the original work of Rienstra [20]. In case of zero mean flow, the following expression for the magnitude of the local mode amplitude $A^{\pm}_{m_c n}(x)$ is obtained by imposing continuity of mode sound power in Eq. (8) (cp. [21] for annular ducts):

$$A^{\pm}_{m_c n}(x) = \sqrt{\frac{\alpha_{m_c n}(\Delta x_{\mathrm{rel}})}{\alpha_{m_c n}(x)} \frac{\phi_a(\Delta x_{\mathrm{rel}})}{\phi_a(x)}} A^{\pm}_{m_c n}(\Delta x_{\mathrm{rel}}) \cdot \exp\left(i \int\limits_{\Delta x_{\mathrm{rel}}}^{x} k^{\pm}_{m_c n}(\breve{x}) \mathrm{d}\breve{x} \right) := T^{\pm}_{m_c n}(x|\Delta x_{\mathrm{rel}}) A^{\pm}_{m_c n}(\Delta x_{\mathrm{rel}}). \tag{14}$$

This expression is valid for cut-on modes only. Partial reflections are neglected as a result of the assumed continuity of sound power for the transmitted modes. Nevertheless, modes propagating in negative axial direction inside the inter-pylon ducts are taken into account, which result from reflection at the pylon trailing edges.

IV. Mode analysis techniques

The microphone arrays in the annular duct and inter-pylon duct in Fig. 2 were designed for the application of mode decomposition techniques. The ring arrays, where the microphones are placed along the circumference at a constant axial position, allow the measured sound field to be broken down into the contributions of modes with different azimuthal mode orders m. However, Azimuthal Mode Analysis does not allow reconstruction of mode amplitudes $A^{\pm}_{mn}$, which are required to compute mode sound power. In order to determine the mode amplitudes, microphones have to be distributed in axial and azimuthal direction, e.g. as shown in Fig. 2.

A. Azimuthal Mode Analysis

Azimuthal Mode Analysis (AMA) is performed by solving a system of linear equations, which is given in matrix formulation as follows:

$$\mathbf{p} = \mathbf{W}_{\mathrm{AMA}}\mathbf{a}_{\mathrm{AMA}}, \tag{15}$$

with sound pressure vector $\mathbf{p} = \{p(\phi_1), \ldots, p(\phi_{N_\phi})\}$, mode amplitude vector $\mathbf{a}_{\mathrm{AMA}}$, and mode transfer matrix $\mathbf{W}_{\mathrm{AMA}}$, whose elements are obtained from Eq. (4) for the annular duct and Eq. (9) for the c-shaped duct. Depending on the sensor arrangement different algorithms exist in literature to solve Eq. (15). The arrays used for Azimuthal Mode Analysis in this study are uniform, i.e. constant spacing between neighboring sensors, allowing the solution of Eq. (15) to be computed by use of the pseudo-inverse $\mathbf{W}^{\dagger} = [\mathbf{W}^H\mathbf{W}]^{-1}\mathbf{W}^H$:

$$\mathbf{a}_{\mathrm{AMA}} = \mathbf{W}^{\dagger}_{\mathrm{AMA}}\mathbf{p}. \tag{16}$$

B. Radial Mode Analysis

In order to determine the sound power transported by cut-on modes inside a duct, Radial Mode Analysis (RMA) has to be performed. The mode amplitudes are reconstructed by fitting the superposition of the pressure distributions corresponding to the acoustic modes (see Eq. (1)) to the measured sound pressure at the microphone array positions. This procedure is written as a system of linear equations in matrix formulation as follows:

$$\mathbf{p} = \mathbf{W}_{\mathrm{RMA}}\mathbf{a}_{\mathrm{RMA}}. \tag{17}$$

In contrast to Eq. (15), the sound pressure vector $\mathbf{p}$ depends on the axial and azimuthal sensor positions. The elements of the mode transfer matrix $\mathbf{W}_{\mathrm{RMA}}$ are composed of the product of the axial and radial mode shape functions $X(x)$ and $R(r)$ in Eqs. (5) and (2) and the azimuthal mode shape function $\Phi(\phi)$ in Eq. (4) or (9) for annular and c-shaped ducts, respectively.

As described in Sec. II, the microphone array installed in the annular duct section was optimized for application of Compressed Sensing-based algorithms [14], such as Block Orthogonal Matching Pursuit (BOMP) (see also [22]). The microphone array in the inter-pylon ducts was not specifically optimized for this application, which can result in a higher sensitivity to disturbing influences like electric noise, resulting from high values of the condition number of the mode transfer matrix $\mathbf{W}_{\mathrm{RMA}}$. To mitigate potentially unstable reconstruction results, an automatized regularization approach is used based on the work of Pereira et al. [23], which yields the regularization parameter β for the regularized pseudo-inverse $\mathbf{W}^{\dagger}_{\mathrm{reg}}(\beta)$:

$$\mathbf{W}^{\dagger}_{\mathrm{reg}}(\beta) := [\mathbf{W}^H\mathbf{W} + \beta^2\mathbf{I}]^{-1}\mathbf{W}^H. \tag{18}$$

To perform Radial Mode Analysis in the inter-pylon ducts, the slowly-varying duct assumption is applied. Therefore, the mode amplitude scaling factor $T^{\pm}_{m_c n}(x|\Delta x_{\mathrm{rel}})$ in Eq. (14) is included for the setup of the mode transfer matrix $\mathbf{W}_{\mathrm{RMA}}$. As a result, the reconstructed mode amplitudes refer to the first axial position where the microphone array detects the propagating wave, i.e. $\Delta x_{\mathrm{rel}} \approx 0.5$ m for modes propagating in positive axial direction and $\Delta x_{\mathrm{rel}} \approx 0.65$ m for modes propagating in negative axial direction (see Fig. 3). The analysis is only performed on cut-on modes. If a mode undergoes cut-off-/cut-on-transition inside the microphone array, it is currently not detected. This limitation may impede the reconstruction of the other cut-on modes due to two aspects. Firstly, according to Eq. (14) the local mode amplitude increases sharply near the transition point. Secondly, these modes are reflected at the pylon trailing edges leading to the development of a standing wave pattern between the transition point and the trailing edge.

V. Results

In this section, results are discussed for target modes $(3,0)$ and $(4,0)$, which were generated by the spinning mode generator in the annular duct section. For each target mode more than 25 individual measurements were performed in the frequency range from about 800 Hz for target mode $(3,0)$ and about 1000 Hz for target mode $(4,0)$ up to 3200 Hz. The measurement data and analysis results, i.e. mode amplitudes and mode sound power, are interpolated to frequencies corresponding to uniformly increasing mode propagation angles between 85 degrees and 25 degrees, which are located close to the excitation frequencies used during the experiment.

A. Assessment of mode synthesis

The spinning mode generator is used to generate single, dominant modes with assigned target azimuthal and radial mode orders, while all other cut-on modes that propagate in the same direction as the target mode are suppressed. Successful mode synthesis is verified by evaluating the target mode dominance, which is defined as the minimum sound power level difference between the target mode and all other cut-on modes propagating in positive axial direction (+). The sound power of the incident modes measured in the annular duct section and the achieved target mode dominance of target modes $(3,0)$ and $(4,0)$ are shown in Fig. 7 for the three pylon configuration. At $\zeta^+_{x;m_a n} = 85°$, the target modes are excited close to their cut-on frequencies with $\alpha_{m_a n} \approx 0.087$. Therefore, these modes transport sound power ineffectively leading to target mode dominance below 10 dB up to $\zeta^+_{x;3,0} = 75°$ and $\zeta^+_{x;4,0} = 70°$. The suppression of the other cut-on modes is overall better for target mode $(3,0)$, because fewer modes are cut-on in comparison to the higher frequencies at which target mode $(4,0)$ is generated. Above 70 degrees, the sound power level differences reach more than 14 dB for target mode $(3,0)$ demonstrating reliable measurement conditions. For target mode $(4,0)$ the target mode dominance reaches about 8 to 12 dB above 70 degrees, which is deemed to be still sufficient for the following analyses.

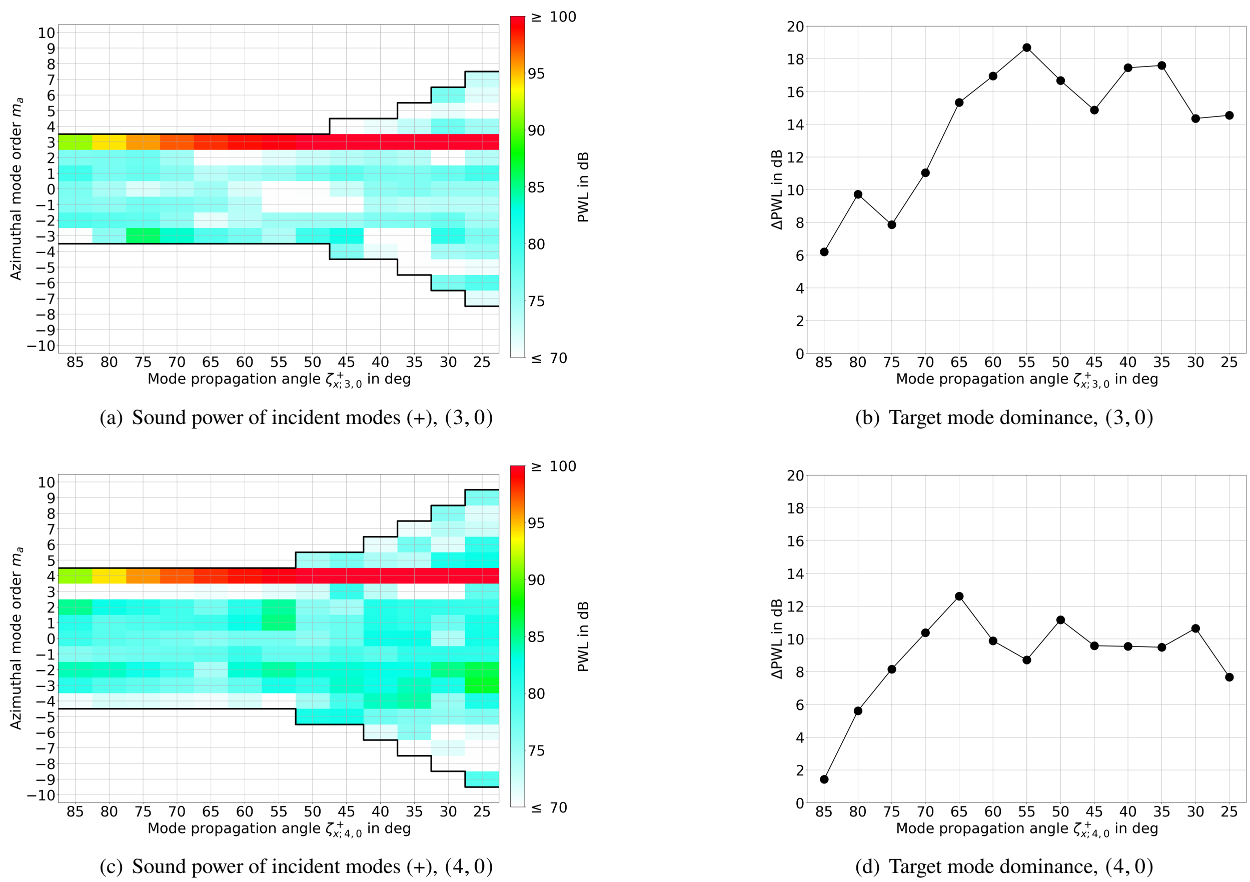

(a) Sound power of incident modes (+), $(3,0)$

(b) Target mode dominance, $(3,0)$

(c) Sound power of incident modes (+), $(4,0)$

(d) Target mode dominance, $(4,0)$

Fig. 7 Mode spectra for excitation of target modes $(3,0)$ and $(4,0)$ and minimum achieved sound power level difference between the target modes and all other cut-on modes propagating in positive axial direction, i.e. target mode dominance. Results are shown for the three pylon configuration.

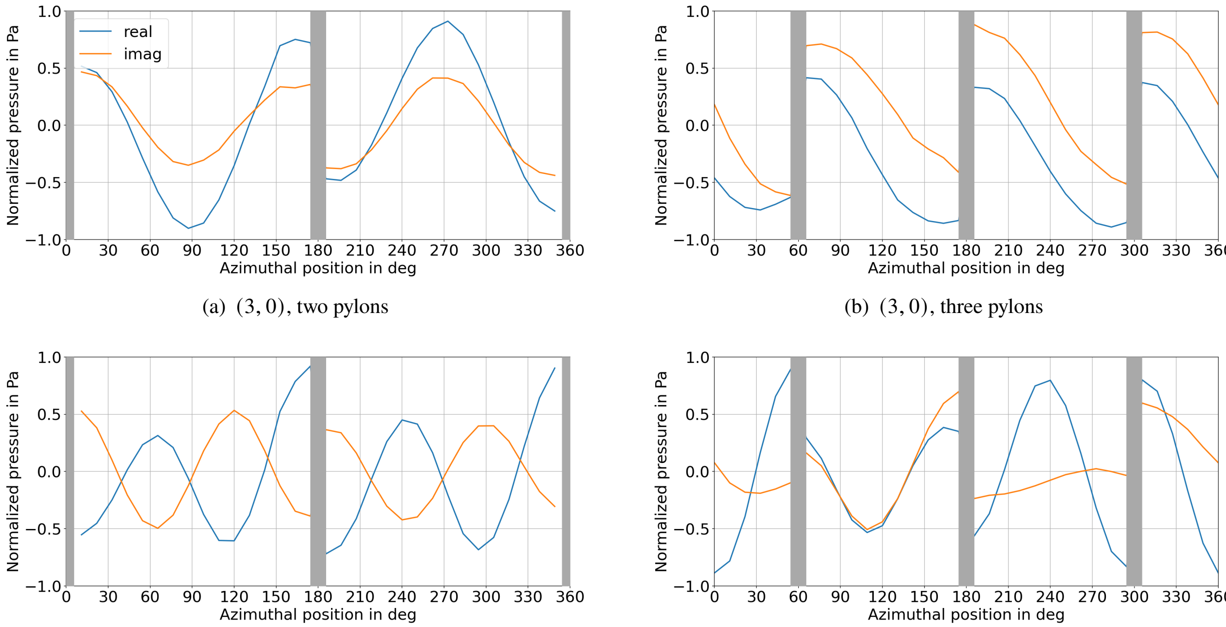

(a) $(3, 0)$, two pylons

(b) $(3, 0)$, three pylons

(c) $(4, 0)$, two pylons

(d) $(4, 0)$, three pylons

Fig. 8 Normalized real and imaginary sound pressure measured using the inter-pylon ring array at $\Delta x_{\mathbf{rel}} \approx 0.65$m. The mode propagation angle is 80 degrees. The positions and width of the pylons are indicated by vertical lines.

B. Azimuthal sound pressure signature in inter-pylon ducts

The complex-valued sound pressure signature in the inter-pylon ducts is shown in Fig. 8 for target modes $(3, 0)$ and $(4, 0)$ and for the two and three pylon configurations. In all cases the mode propagation angle of the target mode in the annular duct is 80 degrees. Cosine-like spatial distributions are observed for each test point confirming the applicability of the c-shaped duct approximation. An important observation emerges from comparing the pressure patterns between neighboring inter-pylon ducts. For the two pylon configuration, the sound fields in the inter-pylon ducts are shifted in phase by 180 degrees if the target mode order m_a is uneven (see Fig. 8a). For even azimuthal mode orders the sound fields in both inter-pylon ducts are in phase (see Fig. 8c). Similarly, the target mode $(3, 0)$ leads to sound fields that are in phase for the three pylon configuration (see Fig. 8b). For this configuration, a phase shift of 120 degrees between the inter-pylon sound fields is observed for target mode $(4, 0)$ (see Fig. 8d).

C. Azimuthal Mode Analysis of the sound field in inter-pylon ducts

The coupling of the acoustic modes in the annular duct to the modes in the inter-pylon ducts is characterized by complex scattering patterns. The azimuthal mode shape function (see Eq. (9)) in the inter-pylon duct describes a standing wave pattern composed of two partial waves traveling in positive and negative azimuthal direction with $\cos\left(m_c \cdot \frac{\pi}{\phi_a}\phi\right) = 1/2\left(\exp(-im_c \cdot \frac{\pi}{\phi_a}\phi) + \exp(im_c \cdot \frac{\pi}{\phi_a}\phi)\right)$. Except for azimuthal mode order $m = 0$, the mode shapes of higher order modes in the annular duct do not match the mode shapes in the inter-pylon duct resulting in scattering into cut-on and cut-off inter-pylon duct modes (see Eq. (13)).

The azimuthal mode spectra using the azimuthal mode shape functions of c-shaped ducts are shown in Fig. 9 for target modes $(3, 0)$ and $(4, 0)$ for both tested pylon configurations. At high mode propagation angles small azimuthal mode amplitudes are measured indicating low mode transmission from the annular duct section into the inter-pylon duct. For decreasing mode propagation angles the sound pressure levels in the inter-pylon duct exhibit an overall increase, but also vary significantly depending on the mode propagation angle. For each target mode, distinct, dominant azimuthal mode orders are excited, which below specific propagation angles agree well with the estimated scattering distribution shown in Fig. 5. Azimuthal mode orders located above the black line are cut-off and are detected predominantly at high mode propagation angles. The other lines indicate the cut-on mode range corresponding to the maximum apex angle

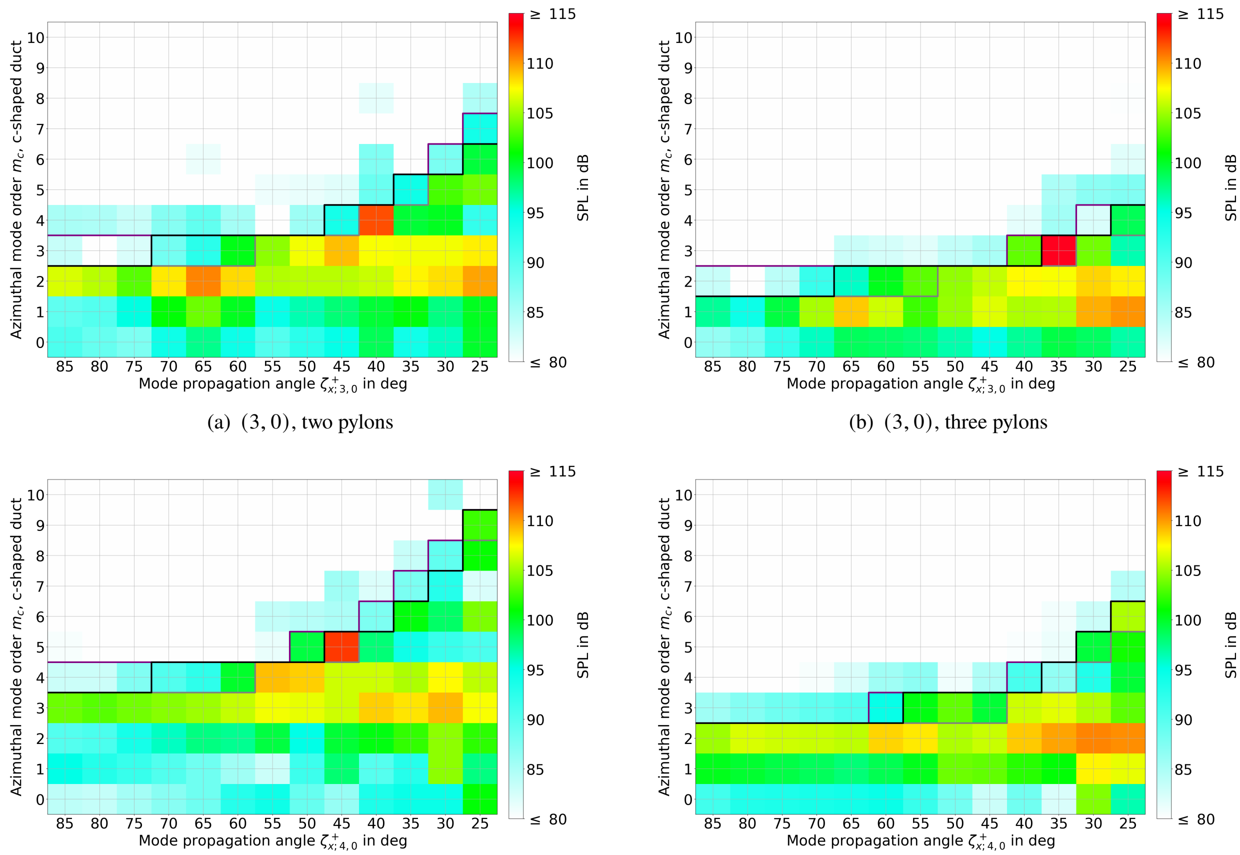

(a) $(3, 0)$, two pylons

(b) $(3, 0)$, three pylons

(c) $(4, 0)$, two pylons

(d) $(4, 0)$, three pylons

Fig. 9 Azimuthal mode amplitudes determined using the azimuthal mode shape functions of c-shaped ducts measured with the inter-pylon ring array at $\Delta x_{\mathrm{rel}} \approx 0.65\mathrm{m}$. The black lines indicate the cut-on mode range at the ring array. The cut-on mode ranges corresponding to the maximum and minimum apex angle of the inter-pylon duct are indicated by purple and gray lines.

(purple, at the pylon leading and trailing edge) and the minimum apex angle (gray, at the point of maximum pylon thickness). The highest mode amplitudes are detected for modes that undergo a double transition from cut-on to cut-off and vice versa in the narrow section of the inter-pylon duct. For example, the target mode $(3, 0)$ at $\zeta^+_{x;3,0} = 40°$ excites the mode $m_c = 4$ in Fig. 9a near its longitudinal resonance resulting from reflection at the mode's second transition point and the pylon trailing edge[†]. Similar conditions occur for modes $m_c = 3$ at $\zeta^+_{x;3,0} = 35°$ in Fig. 9b and $m_c = 5$ at $\zeta^+_{x;4,0} = 45°$ in Fig. 9c.

Figure 10 presents the results of azimuthal mode analysis performed with the microphone ring array at $\Delta x_{\mathrm{rel}} = 0.65\mathrm{m}$ using the azimuthal mode shape functions for annular ducts. With the microphone array being located close to the pylon trailing edges, these mode spectra correspond approximately to the mode distribution that results downstream of the pylon section. The mode spectra show multiple scattered modes for each target mode, which are shifted from the target mode order by multiples of the number of pylons. Mode scattering occurs predominantly into cut-on modes. At few mode propagation angles cut-off modes are excited close to their cut-on frequencies yielding high sound pressure levels.

The most interesting effect is mode reversal, which refers to dominant scattering into the inverted mode order $-m_a$ and was first described by Panek et al. [4]. In the inter-pylon section, mode reversal occurs for both target modes at mode propagation angles between 50 and 30 degrees for the two pylon configuration (see Fig. 10). In the three pylon configuration mode reversal is observed for lower mode propagation angles starting at 35 degrees for target mode

[†]The occurrence of the longitudinal resonances was identified using the mode-matching technique described by Girier et al. [17].

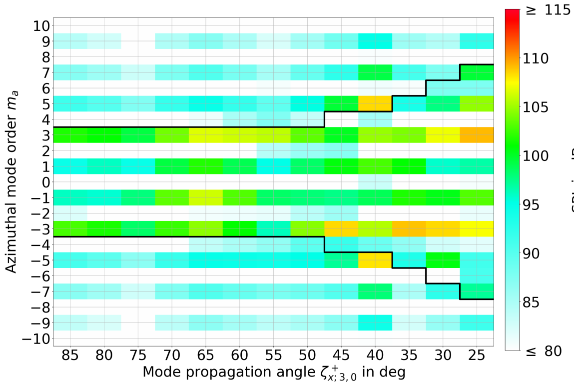

(a) (3, 0), two pylons

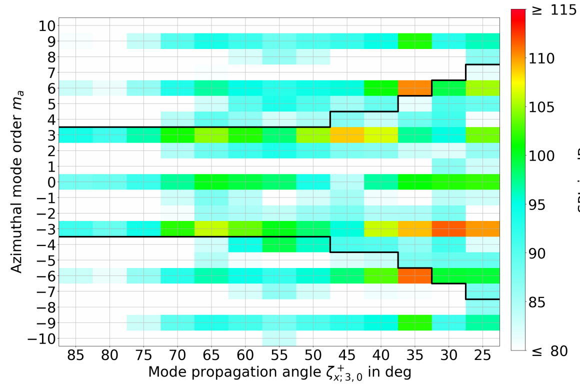

(b) (3, 0), three pylons

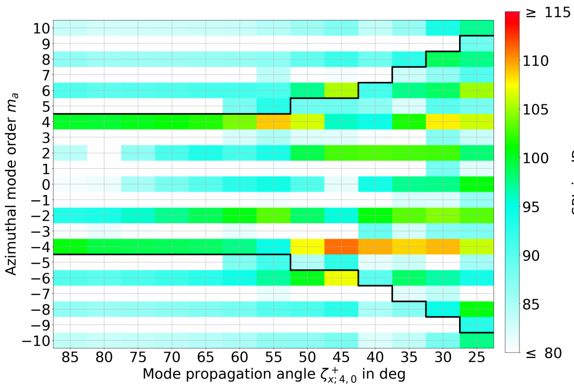

(c) (4, 0), two pylons

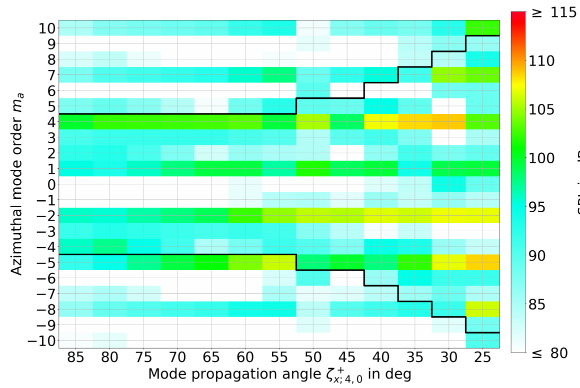

(d) (4, 0), three pylons

Fig. 10 Azimuthal mode amplitudes determined using the azimuthal mode shape functions of annular ducts measured with the full 360 degree inter-pylon ring array at $\Delta x_{\mathrm{rel}} \approx 0.65\mathrm{m}$. These mode spectra correspond approximately to the mode distribution that is radiated downstream of the pylon section. The black line indicates the cut-on mode range in the annular duct.

$(3, 0)$. In this case additionally mode order $m_a = \pm 6$ is excited strongly coinciding with the high sound pressure level of inter-pylon duct mode $m_c = 3$ in Fig. 9b. For target mode $(4, 0)$ mode reversal is not observed for the three pylon configuration, because the reverse mode order $m_a = -4$ is not part of the subset of scattering mode orders. The angles, at which mode reversal is identified, are in good agreement with the theoretical mode reversal angle

$$\zeta_{\mathrm{rev}} = \arctan\left(\frac{\frac{2\pi}{N_{\mathrm{pylon}}} R_o}{L}\right), \tag{19}$$

which is derived from the mode reversal length introduced in [4].

D. Sound power of reflected and transmitted modes

The sound power levels of the reflected modes measured in the annular duct section are depicted in Fig. 11 for target modes $(3, 0)$ and $(4, 0)$ and both pylon configurations. Incident modes at high mode propagation angles are strongly reflected at the pylon section resulting in high sound power levels relative to the low sound power of the target modes close to their cut-on frequencies (see Fig. 7). The results in Figs. 11a-c indicate the occurrence of mode reversal in the reflected sound field, which is identified for propagation angles between 75 and 55 degrees for both pylon configurations. The incident modes and the reverse modes reach higher sound power levels than the other scattering modes with the exception of scattering mode $(-5, 0)$ at $\zeta^+_{x;4,0} = 45°$ in Fig. 11d. At lower mode propagation angles the sound power levels of the reflected modes decrease as a result of increasing transmission into the inter-pylon ducts.

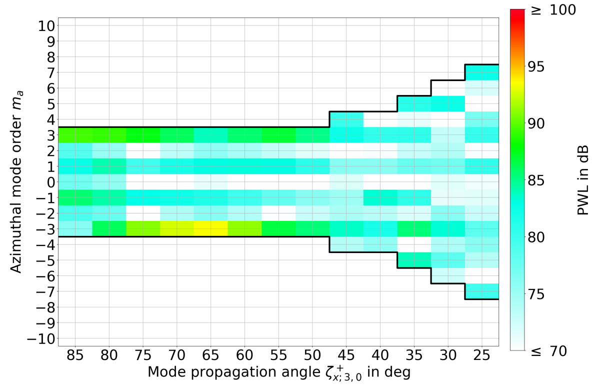

(a) (3, 0), two pylons

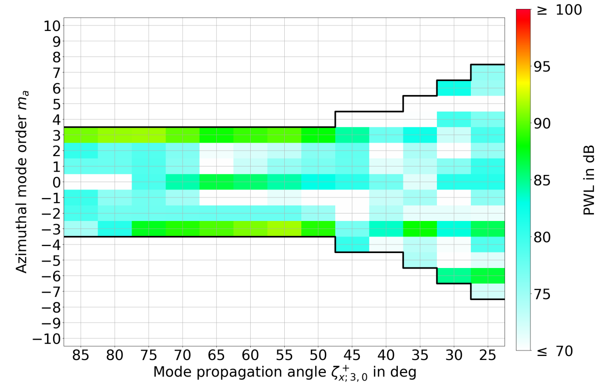

(b) (3, 0), three pylons

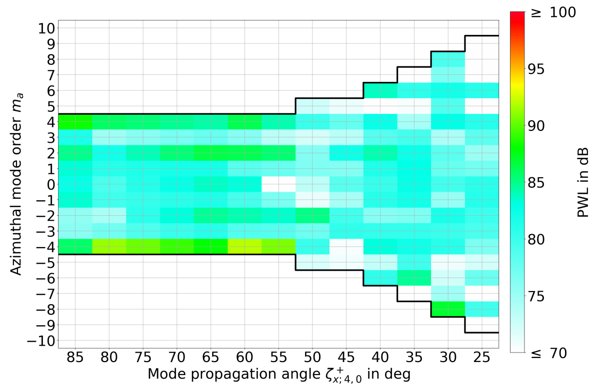

(c) (4, 0), two pylons

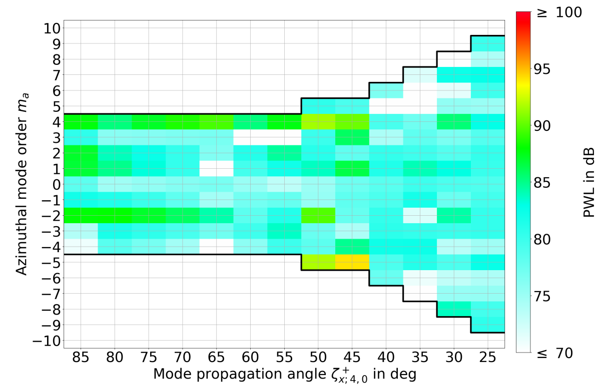

(d) (4, 0), three pylons

Fig. 11 Sound power of reflected radial modes measured in the annular duct section upstream of the pylons. The black line indicates the cut-on mode range.

The mode sound power measured in the inter-pylon duct is shown in Fig. 12. Radial Mode Analysis is performed for the three pylon configuration using the c-shaped duct model in combination with the slowly-varying duct assumption. The sound power spectra of the transmitted modes exhibit the same dominant mode orders as the azimuthal mode spectra in Figs. 9b,d. The sound power levels of the transmitted inter-pylon duct modes in Figs. 12a,c fluctuate with decreasing mode propagation angle. The results in Figs. 12b,d corresponding to the modes, which are reflected at the pylon trailing edge, show generally low sound power levels. High sound power of reflected modes is detected close to the mode cut-on frequency of mode $m_c = 3$ at $\zeta^+_{x;3,0} = 35°$ in Fig. 12b and when the transition point of an inter-pylon duct mode from cut-off to cut-on is located inside the microphone array as indicated by the purple lines (see $m_c = 1$ at $70° \leq \zeta^+_{x;3,0} \leq 60°$ in Fig. 12b and $m_c = 2$ at $\zeta^+_{x;4,0} = 55°$ in Fig. 12d). The latter condition has an impact on the analysis of other cut-on modes, which can impede the accuracy of the determined mode amplitudes and sound power. The sound power balance calculated as the difference between the sound power of the target mode and the reflected and transmitted modes in Fig. 13a confirms an overestimation of the transmitted sound power for target mode $(3, 0)$ exactly in the range of mode propagation angles, at which the transition point of mode $m_c = 2$ is located inside the microphone array, i.e. $70° \leq \zeta^+_{x;3,0} \leq 60°$. Furthermore, the sound power balance shows non-physical, positive values at very high mode propagation angles linked to small axial wave numbers close to the mode cut-on frequencies, where Radial Mode Analysis and mode synthesis using a loudspeaker array are prone to errors. Apart from these critical points, the sound power balance ranges within +/- 1 dB over a wide range of mode propagation angles ($\zeta^+_{x;3,0} \leq 50°$ and $\zeta^+_{x;4,0} \leq 70°$) demonstrating the suitability of the proposed approach for Radial Mode Analysis in the inter-pylon ducts.

In order to assess the characteristic scattering pattern on the basis of mode sound power, similar to the projection value shown in Fig. 5, the sound power levels of all cut-on modes m_c measured in the inter-pylon duct relative to the sound power of the target modes of order m_a at fixed excitation frequencies of 1600 Hz, 2000 Hz, and 2400 Hz are

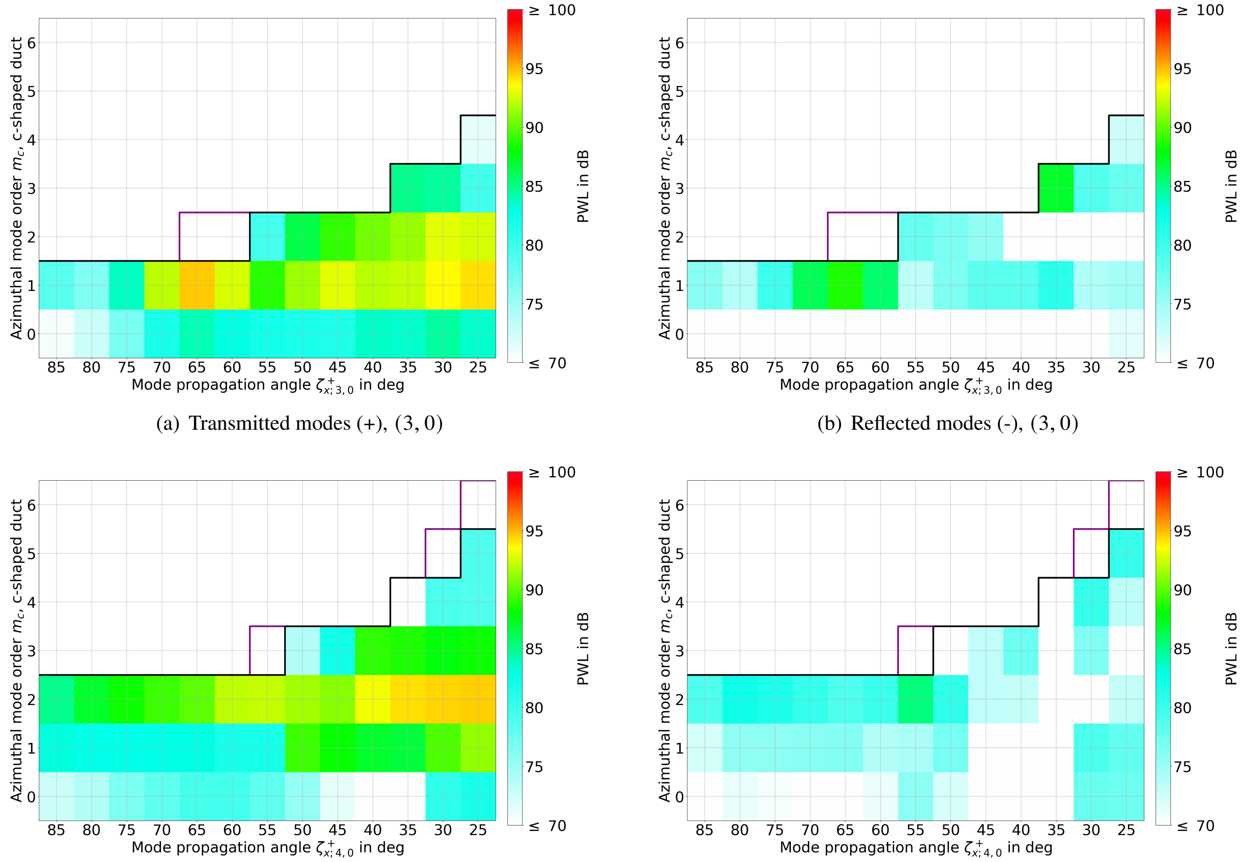

(a) Transmitted modes (+), (3, 0)

(b) Reflected modes (-), (3, 0)

(c) Transmitted modes (+), (4, 0)

(d) Reflected modes (-), (4, 0)

Fig. 12 Radial mode sound power measured in the inter-pylon duct using the mode propagation model for c-shaped ducts. The results are given for the three pylon configuration. The black lines indicate the cut-on mode range according to the smallest (black lines) and the largest (purple lines) apex angle along the axial length of the microphone array.

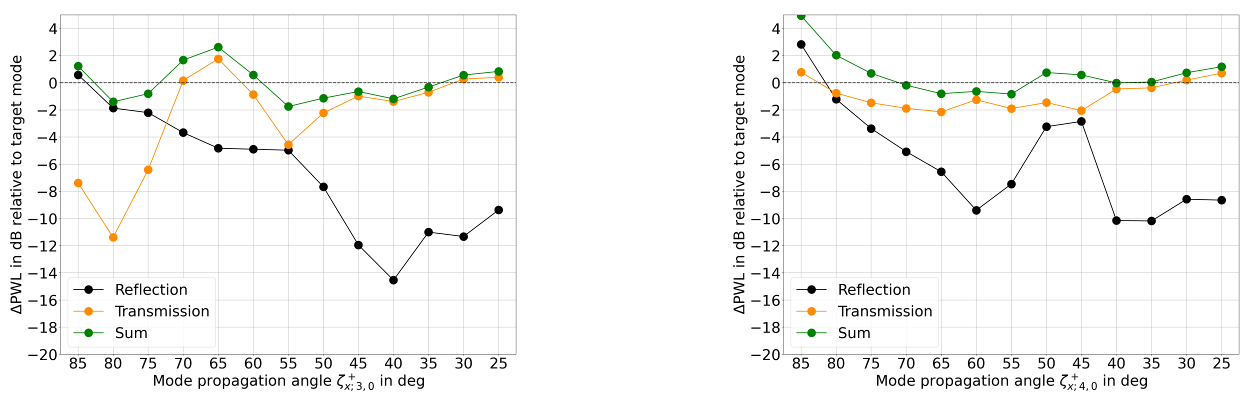

(a) (3, 0)

(b) (4, 0)

Fig. 13 Summed sound power levels of reflected and scattered modes measured in the annular duct and transmitted modes measured in the inter-pylon duct relative to the sound power of the target mode. The results are given for the three pylon configuration.

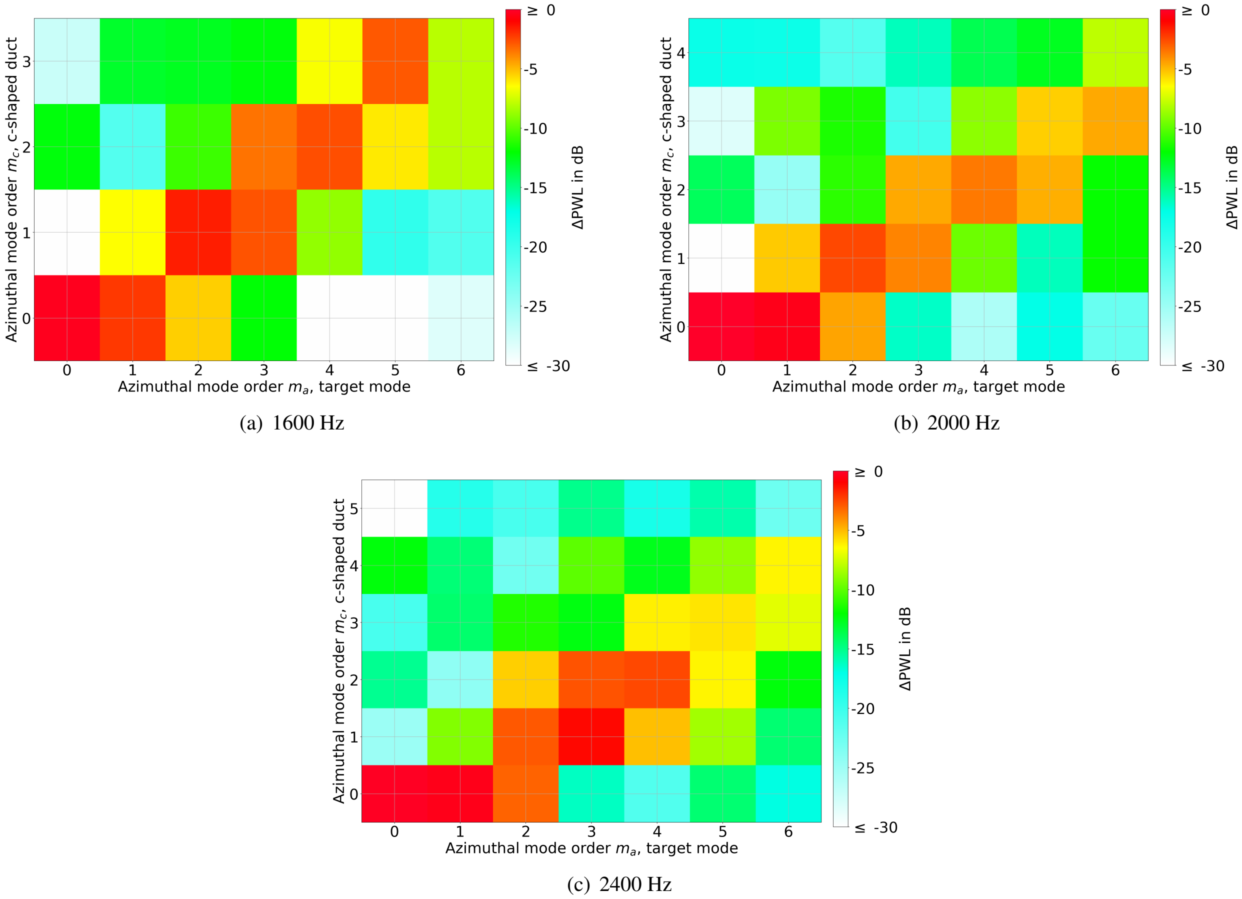

(a) 1600 Hz

(b) 2000 Hz

(c) 2400 Hz

Fig. 14 Distribution of radial mode sound power measured in the inter-pylon duct using the mode propagation model for c-shaped ducts for target modes $(m, 0)$ in the range $m \in [0, \dots, 6]$. Sound power levels are given relative to the target mode in the annular section for the three pylon configuration. The level reduction due to the distribution of sound power over three inter-pylon ducts is compensated.

shown in Fig. 14. The results display characteristic distribution patterns that demonstrate the link between the incoming target mode in the annular duct and dominant inter-pylon duct modes. These characteristic distribution patterns appear to be only weakly frequency-dependent and match remarkably well with the simple estimation in Fig. 14.

VI. Conclusion

Reflection, transmission and scattering of acoustic duct modes at a section with large pylons is investigated using an experimental setup equipped with a spinning mode generator and two microphone arrays. The spinning mode generator consisting of two loudspeaker ring arrays is used to generate single, dominant modes, which allows a detailed assessment of the propagation effects occurring inside the inter-pylon ducts and in the annular duct depending on the mode propagation angle of the target mode. Characteristic phase relations between the sound pressure measured in the neighboring inter-pylon ducts are identified depending on the azimuthal mode order of the target mode and the number of pylons. Mode decomposition in the inter-pylon ducts is facilitated by the assumption of c-shaped and slowly-varying ducts. Azimuthal mode spectra as well as sound power spectra reveal characteristic scattering patterns in the inter-pylon ducts, which are shown to be well approximated by a projection of the azimuthal mode shape functions of the annular duct onto the mode shapes of the c-shaped duct. The results show that sparse, incident mode fields in the annular duct generate sparse mode fields in the inter-pylon ducts. This suggests that sparse mode analysis techniques such as Compressed Sensing based mode analysis can be applied in combination with optimized microphone arrays in bifurcated ducts in the bypass of aircraft engines. The radial mode decomposition inside the inter-pylon duct, which is introduced in this study, yields accurate results over a wide range of mode propagation angles and frequencies. A major limitation of the Radial Mode Analysis in the inter-pylon ducts results from neglecting cut-off modes in the radial mode breakdown, which is shown to affect the analysis of other cut-on modes when the transition point of a mode from cut-off to cut-on is located inside the microphone array. Future studies will investigate an extended radial mode breakdown in the inter-pylon duct by considering the presence and transition of cut-off modes.

Acknowledgments

This research has been performed in the frame of the project COMPANION (COMmon Platform and Advanced iNstrumentration readIness for ultra efficient propulsiON) - Grant Agreement No. 101140627. The project is supported by the Clean Aviation Joint Undertaking and its members. Funded by the European Union. Views and opinions expressed are however those of the author(s) only and do not necessarily reflect those of the European Union or Clean Aviation Joint Undertaking. Neither the European Union nor Clean Aviation JU can be held responsible for them.

The authors thank Léo Girier (INSA Lyon) for his valuable contribution.

companion CLEAN AVIATION Co-funded by the European Union

References

[1] Tyler, J. M., and Sofrin, T. G., "Axial flow compressor noise studies," *SAE Tech. Pap. 620532*, 1962. https://doi.org/10.4271/620532.

[2] Moreau, S., "Turbomachinery noise predictions: present and future," *Acoustics*, Vol. 1, No. 1, 2019. https://doi.org/10.3390/acoustics1010008.

[3] Panek, L., Schoenwald, N., Richter, C., and Thiele, F., "Simulation of the rearward propagation of fan noise through a long cowl aero-engine," *AIAA Paper 2008-2820*, 2008. https://doi.org/10.2514/6.2008-2820.

[4] Panek, L., Schönwald, N., Richter, C., and Thiele, F., "Mode propagation in bifurcated bypass ducts: elementary mechanisms," *AIAA Paper 2010-3894*, 2010. https://doi.org/10.2514/6.2010-3894.

[5] Schönwald, N., Panek, L., Richter, C., and Thiele, F., "Mode propagation in bifurcated bypass ducts: application oriented simulation approach," *AIAA Paper 2010-3895*, 2010. https://doi.org/10.2514/6.2010-3895.

[6] Chen, X., Huang, X., and Zhang, X., "Sound radiation from a bypass duct with bifurcations," *AIAA J.*, Vol. 47, No. 2, 2009, pp. 429–436. https://doi.org/10.2514/1.39710.

[7] Redonnet, S., and Druon, Y., "Computational aeroacoustics of aft fan noises characterizing a realistic coaxial engine," *AIAA J.*, Vol. 50, No. 5, 2012, pp. 1029–1046. https://doi.org/10.2514/1.J050730.

[8] Holewa, A., Weckmüller, C., and Guérin, S., "Impact of bypass duct bifurcations on fan noise," *J. Propuls. Power*, Vol. 30, No. 1, 2014, pp. 143–152. https://doi.org/10.2514/1.B34957.

[9] Zeng, S., Zhang, G., Wang, X., Gao, F., and Sun, X., "Rotor/stator interaction noise prediction in C-shaped duct with lifting surface method," *Journal of Sound and Vibration*, Vol. 615, No. 119175, 2025. https://doi.org/10.1016/j.jsv.2025.119175.

[10] Nark, D. M., Jones, M. G., Kreitzman, J. R., and Schuster, W., "Bypass Duct Acoustic Liner Design With and Without Bifurcation Effects," *AIAA Paper 2024-3250*, 2024. https://doi.org/10.2514/6.2024-3250.

[11] Tapken, U., Bauers, R., Arnold, F., and Zillmann, J., "Turbomachinery Exhaut Noise Radiation Experiments - Part 2: In-Duct and Far-Field Mode Analysis," *AIAA Paper 2012-2858*, 2008. https://doi.org/10.2514/6.2008-2858.

[12] Bauers, R., Stöhr, C., Tapken, U., and Enghardt, L., "Experimental study of acoustic mode transmission through c-shaped bypass-duct sections of aero-engines," *Proceedings of the 16th Congress on Sound and Vibration*, , No. 422, 2009.

[13] Tapken, U., and Behn, M., "Influence of foam-resin lining on the reflections and scattering of acoustic modes at pylons in a flow duct," *Proceedings of DAS|DAGA 2025*, 2025. https://doi.org/10.71568/dasdaga2025.569.

[14] Behn, M., Klähn, L., and Tapken, U., "Comprehensive experimental investigation of mode transmission through stator vane rows: Results and calibration of an analytical prediction model," *23rd AIAA/CEAS Aeroacoustics Conference*, Denver, Colorado (USA), 2017. https://doi.org/10.2514/6.2017-3218.

[15] Knobloch, K., Grizewski, L., Kohlenberg, H.-F., Behn, M., and Genßler, J., "Framework for modal based assessment of liner structures," *AIAA Paper 2024-3298*, 2024. https://doi.org/10.2514/6.2024-3298.

[16] Vincent, H., Pereira, A., Jacob, M. C., Behn, M., and Tapken, U., "Numerical Investigation of Mode Scattering in Bifurcated Annular Ducts," *AIAA Paper*, 2026. Submitted.

[17] Girier, L., Leclère, Q., Behn, M., and Tapken, U., "On a Mode-Matching Technique for Acoustic Scattering by an Annular Row of Airfoil-Shaped Pylons," *AIAA Paper*, 2026. Submitted.

[18] Tapken, U., "Analyse und Synthese akustischer Interaktionsmoden von Turbomaschinen," Dissertation, Technical University Berlin, Berlin, Germany, 2016. https://doi.org/10.14279/depositonce-5124.

[19] Morfey, C., "Rotating pressure patterns in ducts: Their generation and transmission," *Journal of Sound and Vibration*, Vol. 1, 1964. https://doi.org/10.1016/0022-460X(64)90007-0.

[20] Rienstra, S. W., "Sound transmission in slowly varying circular and annular lined ducts with flow," *Journal of Fluid Mechanics*, Vol. 380, 1999, pp. 279–296. https://doi.org/10.1017/S0022112098003607.

[21] Behn, M., Pilgrim, J., and Tapken, U., "Experimental Validation of an Analytical Sound Transmission Model for Fan Stages," *30th AIAA/CEAS Aeroacoustics Conference*, Rome, Italy, 2024. https://doi.org/10.2514/6.2024-3271.

[22] Eldar, Y. C., "Block-Sparse Signals: Uncertainty Relations and Efficient Recovery," *IEEE Transactions on Signal Processing*, Vol. 58, No. 6, 2010, pp. 3042–3054.

[23] Pereira, A., Antoni, J., and Leclère, Q., "Empirical Bayesian regularization of the inverse acoustic problem," *Applied Acoustics*, Vol. 97, 2015, pp. 11–29. https://doi.org/10.1016/j.apacoust.2015.03.008.